Single-molecule tracking of mRNA exiting from RNA polymerase II

Joanna Andrecka*†, Robert Lewis*†, Florian Brückner*‡, Elisabeth Lehmann*‡, Patrick Cramer*‡, and Jens Michaelis*†§

*Munich Center for Integrated Protein Science (CiPS^{M}) and Center for Nanoscience (CeNS), Ludwig-Maximilians-Universität München, 81377 Munich, Germany; †Department of Chemistry and Biochemistry, Ludwig-Maximilians-Universität München, Butenandtstrasse 11, 81377 Munich, Germany; and ‡Gene Center Munich and Department of Chemistry and Biochemistry, Ludwig-Maximilians-Universität München, Feodor-Lynen-Strasse 25, 81377 Munich, Germany

Edited by Steven M. Block, Stanford University, Stanford, CA, and approved November 5, 2007 (received for review April 25, 2007)

Single-pair fluorescence resonance energy transfer was used to track RNA exiting from RNA polymerase II (Pol II) in elongation complexes. Measuring the distance between the RNA 5′ end and three known locations within the elongation complex allows us determine its position by means of triangulation. RNA leaves the polymerase active center cleft via the previously proposed exit tunnel and then disengages from the enzyme surface. When the RNA reaches lengths of 26 and 29 nt, its 5′ end associates with Pol II at the base of the dock domain. Because the initiation factor TFIIB binds to the dock domain and exit tunnel, exiting RNA may prevent TFIIB reassociation during elongation. RNA further extends toward the linker connecting to the polymerase C-terminal repeat domain (CTD), which binds the 5′-capping enzyme and other RNA processing factors.

Pol II | transcription | FRET | triangulation | fluorescence

Pol II synthesizes all eukaryotic mRNA and comprises 12 subunits, Rpb1 to Rpb12. An atomic model of Pol II has been obtained by x-ray crystallography (1, 2). Additional studies of Pol II–nucleic acid complexes have given insights into the elongation complex structure and molecular aspects of the transcription mechanism (3–7). Crystallographic analysis detected the position of the nascent RNA within the DNA–RNA hybrid above the active site (positions +1 to −8, with +1 denoting the nucleotide addition site) and for 2 nt upstream of the hybrid after the point of DNA–RNA strand separation (positions −9 and −10) (3, 7). The last-ordered RNA nucleotide is located at the entrance to a tunnel [called the RNA exit channel for the bacterial RNA polymerase (8)], which is formed among the polymerase wall, clamp, and lid. This tunnel leads from the active center cleft to the exterior and was proposed to accommodate exiting RNA (1, 3, 6, 7). Beyond the putative exit tunnel, two prominent surface grooves on either side of the dock domain in principle could further accommodate exiting RNA (1, 9). Groove 1 winds along the base of the clamp toward the Rpb4/7 subcomplex, whereas groove 2 leads along Rpb11 toward Rpb8. Recently, nascent RNA could be cross-linked to Rpb7, providing apparent support for groove 1 (10). RNA beyond position −10 was present in one of the crystallographic studies of the elongation complex (3) but could not be observed in the tunnel or in the subsequent grooves, suggesting that its interactions, if they exist, are transient and cannot be detected in medium-resolution electron density maps.

To study if the nascent RNA indeed exits through the proposed tunnel, and whether it follows a defined surface path beyond the tunnel, we used single-molecule fluorescence experiments. Single-particle methods prevent the loss of information because of averaging that is inherent to bulk experiments and crystallography (11–14). Fluorescence resonance energy transfer between two fluorophores [single-pair (sp)-FRET] provides a very sensitive tool for studying distances and conformational changes within biological complexes in the range of 10–100 Å (15, 16).

Here we used sp-FRET to infer the position of the 5′ end of the nascent RNA by relative distance measurements to known positions in the Pol II elongation complex. In a process known as triangulation/trilateration, we determined a previously unknown location by measuring the distance to that position from at least three known points in space. This process allowed us to map the path of the exiting RNA upstream of position −10. In this article, implications of our work for understanding the transcription mechanism are discussed.

Results

Engineering Fluorophore-Labeled Active Pol II Elongation Complexes. The possibility to assemble complete Pol II elongation complexes from endogenous yeast 10-subunit core enzyme, recombinant Rpb4/7 subcomplex, and synthetic nucleic acid scaffolds (3) enabled the preparation of defined elongation complexes with fluorescent labels at discrete positions. Labels were readily incorporated into the synthetic nucleic acids. To reliably predict label locations, we used nucleic acid scaffolds that closely resemble those in the complete Pol II elongation complex structure (3). We prepared scaffolds with different RNA lengths, ranging from 17 to 35 nt and comprising a donor tetramethylrhodamine (TMR) fluorophore at their 5′ ends (RNA17, RNA20, RNA23, RNA26, RNA29, RNA32, and RNA35; Fig. 1 and *Materials and Methods*). An acceptor fluorophore (Alexa 647) was attached to the DNA template strand either at position −10 (DNA1) or position +3 (DNA2). A third acceptor label was coupled to an accessible cysteine residue in the Rpb4/7 complex (Rpb7–C150; Fig. 1 and *Materials and Methods*) after other cysteines had been replaced by serines with the use of site-directed mutagenesis in *Escherichia coli*.

The resulting elongation complexes allowed us to localize the RNA 5′ end at various positions and thus to map the path that the growing RNA chain follows when exiting the polymerase. The complexes are active in RNA chain elongation in ensemble (17) and single-molecule experiments [see supporting information (SI) Fig. 5]. They may therefore be viewed as stable intermediates in the early elongation process.

sp-FRET Analysis. Using a single-molecule fluorescence microscope, we measured sp-FRET signals from individual elongation complexes (*Materials and Methods*). We recorded the fluorescence intensities of donor and acceptor molecules as a function of time. With these trajectories, we computed the respective sp-FRET efficiencies. Using the data from many molecules, we then constructed histograms of FRET efficiencies. For each length of RNA, we performed three independent sets of experiments measuring the FRET efficiency of complexes with the donor molecule attached to

Author contributions: J.A., F.B., P.C., and J.M. designed research; J.A., R.L., F.B., E.L., P.C., and J.M. performed research; F.B., E.L., P.C., and J.M. contributed new reagents/analytic tools; J.A., R.L., F.B., P.C., and J.M. analyzed data; and J.A., R.L., F.B., E.L., P.C., and J.M. wrote the paper.

The authors declare no conflict of interest.

This article is a PNAS Direct Submission.

§To whom correspondence should be addressed. E-mail: michaelis@lmu.de.

This article contains supporting information online at www.pnas.org/cgi/content/full/0703815105/DC1.

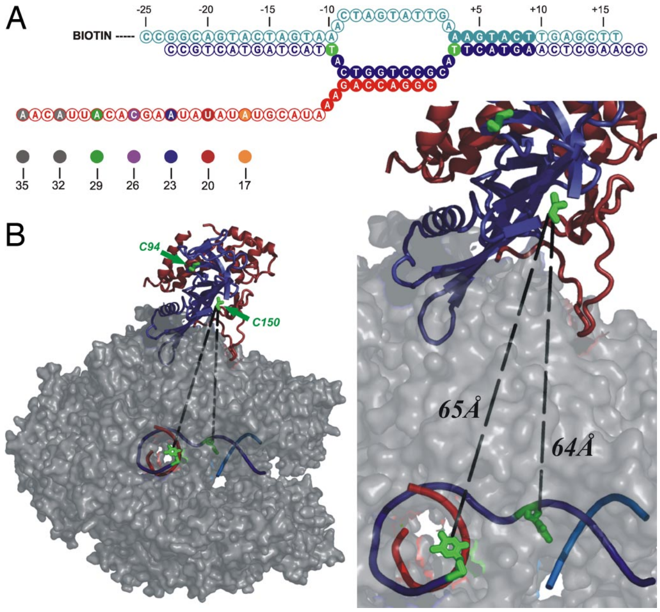

Fig. 1. Pol II structure and labeling. (*A*) Schematic showing the oligonucleotides used in the single-molecule experiments for the formation of elongation complexes. Filled and open circles denote nucleotides whose positions are known and unknown, respectively, from crystallographic studies (3). Highlighted are the labeling positions on the template DNA and RNA. (*B*) Top view of the complete Pol II elongation complex structure (3), indicating labeling sites. The core polymerase is shown in surface representation (in gray), and the backbone of the template DNA (blue), nontemplate DNA (cyan), and RNA (red) and the heterodimer Rpb4/7 (Rpb4 in red and Rpb7 in blue) are displayed with cartoon diagrams. The positions that were used to attach dye molecules, that is, Rpb7, residues Rpb7–C94, and Rpb7–C150, as well as the template DNA at position −10 (DNA1) and +3 (DNA2), are shown in green. At *Right* is a close-up view of the labeling region highlighting the distances between Rpb7–C150 and DNA1 as well as Rpb7–C150 and DNA2.

the RNA 5′ end and the acceptor to DNA1, DNA2, or Rpb7–C150. Fig. 2 shows as examples sp-FRET histograms for elongation complexes containing DNA1 and RNA17 as well as DNA1 and RNA26, together with characteristic time trajectories of donor fluorescence, acceptor fluorescence, and computed sp-FRET efficiencies. All other histograms are shown in the supporting information (SI Figs. 6 and 7). The main results are summarized in Table 1.

The trajectory of FRET efficiency *E* shown in Fig. 2*A* is rather constant, which is the typical behavior observed for all elongation complexes with RNA17, RNA20, or RNA23. In contrast, when the RNA is extended from 23 to 26 nt, the FRET signal no longer remains constant. A typical example is shown in Fig. 2*C*: the FRET efficiency of the DNA1–RNA26 elongation complex switches repeatedly between two levels, and the corresponding histogram shows two peaks (Fig. 2*D*). Such apparent fluctuations could be caused by either distance variations or photo-physical changes in the donor and/or acceptor molecule. We checked for changes in the acceptor brightness by exciting the acceptor directly in an alternating excitation scheme (18, 19). A typical example of a trajectory showing strong modulation of the FRET efficiency when being excited with green light and constant fluorescence intensity when excited with red light is shown in Fig. 3. We furthermore analyzed the total intensity of emitted fluorescence and found that the observed fluctuations are not caused by changes of donor brightness (SI Fig. 8). Thus, the observed fluctuations of *E* cannot be attributed to photo-physical changes of the donor or acceptor molecule, instead our single-molecule probe reports on a real-time reordering of the growing RNA chain, with an apparent rate of reordering of $\approx 1\ s^{-1}$.

In a next step, we used the mean FRET efficiencies (*E*) (extracted from the histograms) to compute distances (*d*) by using the determined Förster distances (*Materials and Methods*). Then, for each length of RNA, we determined the distance of its 5′ end to the three known points in space (DNA1, DNA2, and Rpb7–C150) by using the respective mean FRET efficiencies extracted from the recorded histograms (Table 1). To infer the unknown relative position of the dye molecule, we constructed a sphere around each of the three known positions with a radius determined by the FRET measurement. The intersection point of the three spheres determines the unknown position. A similar procedure has been applied previously to the study of helicase–DNA complexes (20).

Accurate Localization of the RNA 5′ End. To test the accuracy of our method, we compared distances computed from sp-FRET measurements to distances within the crystallographic structure. The mean FRET efficiencies of a donor molecule on DNA1 or DNA2 and an acceptor on Rpb7–C150 resulted in distances of 61 Å and 63 Å, respectively (SI Fig. 9). These distances are in good agreement with the values of 65 Å (DNA1) and 64 Å (DNA2) in the crystal structure [PDB code 1Y1W (3)].

It is known that a TMR fluorophore attached to the 5′ end of DNA via a flexible six-carbon linker usually is stacked on top of the last base within the nucleic acid helix (21). Although in case of RNA, these interactions might be weaker, stacking of the dye molecule to the last base of the RNA still is the most likely conformation. Thus, the dye molecule is expected to sit in close proximity to the last base and therefore can report accurately on the position of the RNA. Although an interaction between the charged surface of the polymerase and the dye molecule attached to its 5′ end in principle could influence the position of the RNA, no systematic effect was observed (SI Fig. 10). However, we cannot rule out the possibility that such a direct interaction between dye molecule and protein surface exists.

Moreover, we checked the determined position by measuring the distance to yet another known point within the structure. To this end, we used another single-cysteine mutant of Rpb7—namely, Rpb7–C94 (Fig. 1)—and measured the distance between the acceptor attached to this position and the donor on the RNA. The measured distance then could be compared with the distance between the intersection point determined by our triangulation (using DNA1, DNA2, and Rpb7–C150) and the position of Rpb7–C94 from the x-ray structure. The comparison yielded deviations of on average 2.5 Å (never >5 Å; SI Table 2), thus providing another estimate of our experimental error.

Furthermore, trilateration allows for a self-consistent test for the accuracy of the sp-FRET distance determination. If one determines four distances, as described above, one can perform four independent three-distance trilaterations and compare the resulting four intersection points. An example of this procedure for the case of RNA29 is shown in SI Fig. 11. The four positions that are determined by the four trilaterations are all within ≈3 Å from each other, thus providing another indication for the accuracy of our method.

RNA Traverses the Exit Tunnel and Disengages from the Surface. Trilateration analysis for RNA17, RNA20, and RNA23 yields the corresponding positions of the 5′ end (Fig. 4). To account for experimental errors, the positions are represented by spheres with a radius of 5 Å (see *Materials and Methods*). The 5′ end of the RNA17 is located near the end of the proposed exit tunnel (Fig. 4*A*). Modeling shows that this position of RNA17 5′ end can only be explained if the RNA extends from the crystallographically observed position −10 through the previously proposed exit tunnel beneath the polymerase lid (Fig. 4). Thus, these data confirm that the RNA leaves the Pol II core through the exit tunnel as had been shown previously for the bacterial RNA polymerase (8, 22). The distance between the last nucleotide visible in the crystal structure

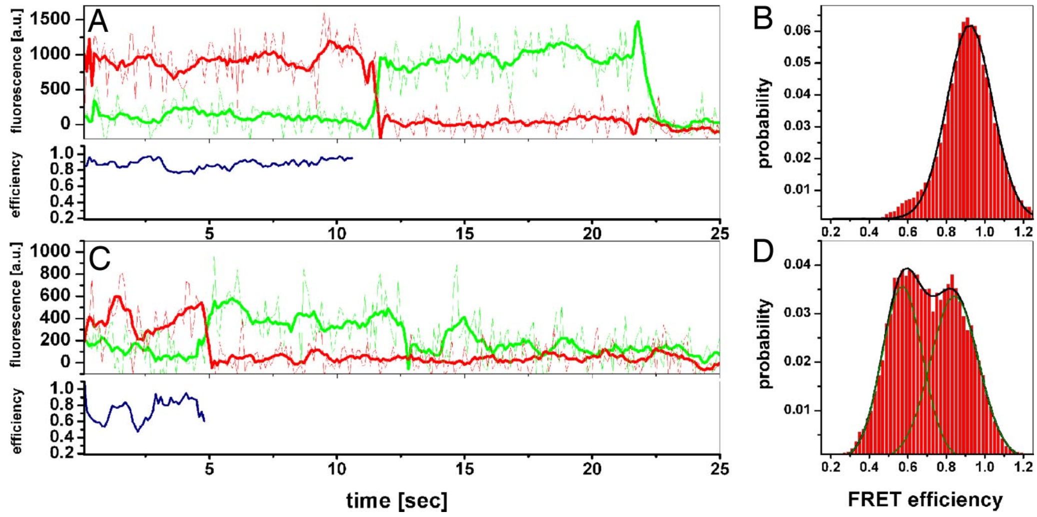

Fig. 2. sp-FRET time traces and histograms. Exemplary time traces and complete histograms for the FRET pairs DNA1–RNA17 (*A* and *B*) and DNA1–RNA26 (*C* and *D*). The time traces show the fluorescence intensities of the donor (green) and the acceptor (red) (thin lines correspond to the actual signal and thick lines correspond to a 10-point sliding average) as well as the computed FRET signal (blue). (*A*) The trajectory of the RNA17–DNA1 pair shows constant fluorescence intensities for the donor and acceptor molecules until bleaching of the acceptor after ≈12 s. At this point, the donor intensity increases and remains constant until the donor itself photo-bleaches after ≈22 s. The computed FRET efficiency is constant, except for small fluctuations attributable to photon-counting noise. (*B*) The histogram of 337 such sp-FRET trajectories shows a single peak, which can be fitted with a Gaussian distribution that is centered at $E = 0.92$. In contrast, the FRET efficiency in *C* for the DNA1–RNA26 sample is not constant but varies between $E \approx 0.85$ and $E \approx 0.6$. Accordingly the histogram in *D* of 224 such trajectories can be fitted with two Gaussian fits centered at $E = 0.58$ and $E = 0.85$.

at position −10 and the observed position at −17 is ≈28 Å, indicating that the RNA is in a stacked conformation within the exit tunnel as was observed recently in the crystal structure of an elongation complex of a bacterial RNA polymerase (22). Beyond the tunnel, for the lengths of 17–23 nt, the RNA is compact and the distance between RNA17 and RNA23 is only ≈11 Å. In this region, the RNA end is too far from the polymerase surface for direct interactions (Fig. 4*B*).

Extending RNA Associates with Pol II Before It Becomes Flexible. For elongation complexes containing RNA26, the single-molecule FRET measurements resulted in histograms that could be fitted with a double Gaussian fit (Fig. 2*D*), thus yielding two values for *d*. Therefore, trilateration does not yield a single position but two positions between which the RNA end is fluctuating (Fig. 4).

Although for short lengths, the RNA lacks contact with the surface of the polymerase, at a length of 26 nt, the RNA associates

Table 1. Overview of the results of the sp-FRET measurements

Donor (TMR)	Acceptor (Alexa 647)	FRET, %	Width	R_0, Å*	Distance, Å	No. of molecules
RNA17	DNA1	92.1	0.24	57	38	337
RNA17	DNA2	55.8	0.19	57	55	336
RNA17	Rpb7–C150	69.1	0.28	59	52	323
RNA17	Rpb7–C94	68.7	0.38	60	52	91
RNA20	DNA1	87.0	0.21	60	43	227
RNA20	DNA2	49.6	0.19	60	60	412
RNA20	Rpb7–C150	67.9	0.23	62	55	226
RNA20	Rpb7–C94	63.8	0.2	63	57	76
RNA23	DNA1	81.4	0.19	59	46	356
RNA23	DNA2	43.3	0.14	59	62	361
RNA23	Rpb7–C150	69.1	0.3	62	54	230
RNA23	Rpb7–C94	67.4	0.23	62	55	105
RNA26†	DNA1	57.8/84.6	0.21/0.23	53	50/40	224
RNA26†	DNA2	42.3/58.8	0.19/0.35	53	55/50	272
RNA26†	Rpb7–C150	55.9/85.5	0.25/0.29	55	53/41	96
RNA26†	Rpb7–C94	50.0/79.3	0.28/0.2	55	55/44	92
RNA29	DNA1	67.2	0.18	62	55	305
RNA29	DNA2	42.7	0.18	62	65	374
RNA29	Rpb7–C150	59.4	0.19	65	61	148
RNA29	Rpb7–C94	51.2	0.17	66	65	96
DNA1	Rpb7–C150	56.2	0.24	63	61	281
DNA2	Rpb7–C150	50.6	0.36	63	63	50

The displayed values are the results of fits of single Gaussian distributions (double Gaussian distributions where indicated) to the experimentally recorded histograms of sp-FRET efficiencies, with the width given by the standard deviation.
*Accuracy ± 2 Å.
†Two peaks found.

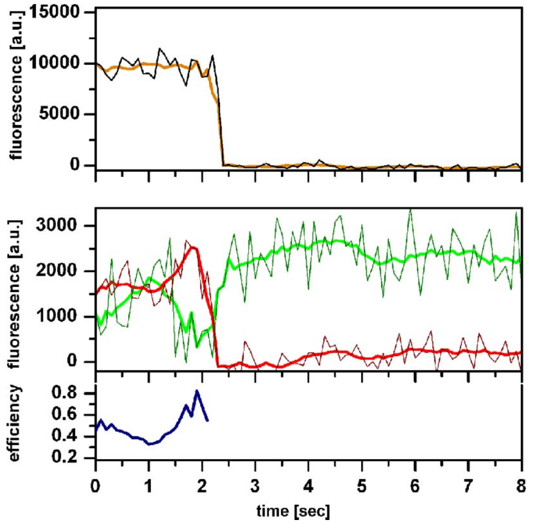

Fig. 3. Alternating laser excitation. The graph shows an exemplary time trace of the DNA1–RNA26 sample. The excitation laser was alternated frame by frame between 633 nm (direct–acceptor excitation, *Upper*) and 532 nm (FRET excitation, *Lower*) (34). Actual data and a 10-point sliding average are shown as thin and thick lines, respectively.

with the surface of the polymerase in the region of the dock domain (Fig. 4). Furthermore, the conformation of the RNA between positions −23 and −29 is more extended, because the 5′ end of RNA26 is located 15 Å or 20 Å from the end of RNA23 and it advances another 17 Å or 21 Å between the positions −26 and −29.

For the even longer RNA32 and RNA35, the histograms can no longer be fitted with a single or double Gaussian fit (SI Fig. 12). The 5′ end is flexible and no longer occupies well defined locations on the Pol II surface.

Discussion

We have used single-particle fluorescence spectroscopy to map the path of mRNA exiting from Pol II. RNA exits from the active center cleft by traversing the previously proposed exit tunnel. RNA then continues toward the dock domain without apparent polymerase interactions. Once the RNA has reached a length of 26 nt, it makes direct contact with the dock domain, following a path between the two grooves previously proposed to possibly accommodate RNA. RNA further extends toward the beginning of the linker that connects to the CTD.

The position of the 5′ end of RNA17 determined here, in comparison with the RNA position at register −10 observed in the crystal structure, shows that the RNA traverses the proposed exit tunnel. It has long been known that single-stranded RNA interacts with polymerase around positions −8 to −15 and that this upstream RNA-binding site contributes to elongation complex stability (23). Our data provide further evidence that the region in the exit tunnel acts as the previously proposed RNA binding site (23).

As the RNA grows longer, the single-particle data reveal a change from a compacted RNA structure (RNA17–RNA23) to a more extended structure (RNA26–RNA29). The RNA apparently lacks direct contacts with the polymerase beyond the tunnel but reassociates with the enzyme surface at register −26 and remains surface-associated at register −29. Reassociation of the RNA may account for sequence-independent transcriptional pausing that had been observed previously at around register −25 (24). Polymerase association of the RNA around registers −26 and −29 also may account for the prevention of transcript slippage at these transcript lengths (25). Previous biochemical studies also have shown indications for an interaction between polymerase and RNA at these transcript lengths (26). When the RNA reaches lengths of 32 and 35 nt, its 5′ end becomes increasingly flexible, and more transient interactions with the polymerase surface are detected in our FRET data. This finding is consistent with an accessibility of the RNA 5′ end to the 5′-capping enzyme, which modifies the RNA end when a length of ≈30 nt is reached (27).

Our observations have further implications for understanding the transition from transcription initiation to elongation. In an initially transcribing complex, growing RNA sterically clashes with the initiation factor TFIIB finger domain (28). Beyond the tunnel, RNA also clashes with the TFIIB ribbon domain (29), which is located on the Pol II dock forming contacts with Rpb1 between

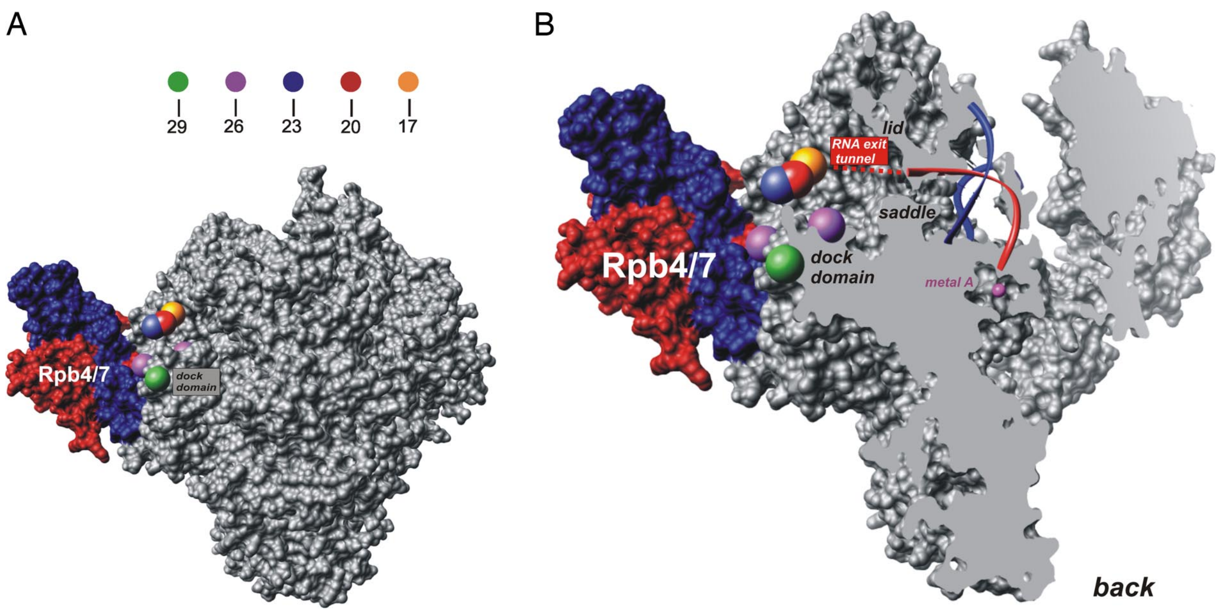

Fig. 4. The position of the nascent RNA within the elongation complex as determined from sp-FRET measurements. (*A*) Back view of the elongation complex. The position of the dye molecule attached to the 5′ end is illustrated by a single sphere with a radius of 5 Å for RNA17 (orange), RNA20 (red), RNA23 (blue), and RNA29 (green) and by a pair of spheres for RNA26 (purple), indicating the presence of two states. (*B*) Cut-away view revealing the paths of the RNA on the interior and exterior. This figure was prepared using UCSF Chimera (46).

residues 409 and 419 (28). Both of the observed positions of RNA26 are exactly in that area, in close proximity to the side chains of serine S409 and arginine R416, respectively. Moreover, the surface charge distribution of the polymerase in the region of the dock domain has both positive and negative patches, providing several possible electrostatic interaction sites (SI Fig. 10). Thus, growing RNA may contribute to TFIIB release during the transition from initiation to elongation, although strain that accumulates during initial DNA scrunching and subsequent bubble collapse is apparently more important (30, 31). Because RNA extends over the dock domain, and not via the flanking grooves, it can prevent reassociation of the TFIIB ribbon with Pol II during mRNA elongation. We confirmed this competition in additional experiments where we added excess amount of TFIIB (see *SI Text*). Even a 100-fold excess of TFIIB leads to the displacement of only a small fraction of the RNA, whereas in the vast majority of ≈80% of the complexes the RNA remains associated with the dock domain (SI Fig. 13). These experiments clearly reveal the potential of our method as it allows for a direct observation of the presence of transcription factors within active elongation complexes and their effect on the location and conformation of the nascent RNA.

A more general implication of this work is that the applied single-molecule trilateration technique based on multiple FRET measurements (20) provides an accurate tool for determining the positions of flexible domains in large multiprotein complexes. For smaller proteins, a related single-molecule approach—namely, mechanical triangulation—recently has been established (32). In particular, we show that single-molecule fluorescence analysis can reveal structural features of a eukaryotic multisubunit RNA polymerase that had thus far escaped detection by x-ray crystallographic means because of inherent flexibility and/or because of limited diffraction data resolution.

The power of single-molecule fluorescence techniques for transcription studies had so far been demonstrated only for bacterial RNA polymerase (31, 33–35). On the other hand, single-molecule force spectroscopy has been used to study the dynamics of transcription by bacterial and viral RNA polymerases. These experiments could elucidate kinetic aspects (36), transcriptional pausing and backtracking (37, 38), and details of the translocation mechanism (39–42). The experiments described in this article, in combination with recently published mechanical studies of Pol II transcription elongation (43), provide a foundation for future single-molecule experiments on eukaryotic RNA polymerases. The time resolution of single-molecule fluorescence experiments allows for an investigation of structural changes in real time, resulting in a dynamic view of complex biological processes. Such experiments could provide valuable insights into unclear mechanistic aspects of eukaryotic transcription and eventually also its regulation.

Materials and Methods

Single-Cysteine Rpb4/7 Variants. The yeast heterodimer of Rpb4/7 was expressed in a bacterial expression system and added to the 10-subunit Pol II–core–nucleic acid scaffold complex *in vitro* to obtain the complete polymerase II elongation complex (3). The comparatively small Rpb4/7 heterodimer with only five native cysteines is well suited for mutagenesis, and therefore the attachment of a single dye molecule within an elongation complex at a well defined and known location becomes feasible. To this end, we performed site-directed mutagenesis replacing native cysteines with serines to produce two mutants with only one single-cysteine residue at locations C94 and C150, respectively. The constructs were expressed and purified as described previously (3).

Dye labeling of the single-cysteine mutants was conducted with an 8 to 10 times molar excess of Alexa 647-C2-Maleimide (Molecular Probes) in DTT free-assembly buffer (50 mM Hepes, pH 7.5/40 mM $(NH_4)_2SO_4$/10 μM $ZnCl_2$/5% glycerol) at 37°C for 1 h. Labeled protein was purified by using G-50 spin-columns (Amersham Biosciences) with assembly buffer (50 mM Hepes, pH 7.5/40 mM $(NH_4)_2SO_4$/10 μM $ZnCl_2$/5% glycerol/10 mM DTT).

Preparation of Pol II Elongation Complexes. Synthetic nucleic acid scaffolds were constructed from RNA and DNA oligomers (Biomers) by using partially mismatched DNA template and nontemplate strands. The sequences of the template and nontemplate strands as well as the RNA sequence (35-nt RNA) are shown in Fig. 1*A*. One should note that no backtracking has been observed for these elongation complexes in multiple crystallographic and biochemical studies in contrast to studies with native promoter sequences, presumably because of energetic penalties caused by the mismatches of the oligonucleotides.

Seven different RNA molecules with lengths from 17 to 35 nt and sequence 5′-AACAUUACACGAAUAUAUAUGCAUAAAGACCAGGC-3′ were investigated (the underlined letters correspond to the seven different 5′ ends of a 17-nt, 20-nt, 23-nt, 26-nt, 29-nt, 32-nt, and 35-nt strand). Each 5′ end had a 6-TMR molecule attached via a C6-amino linker. The nontemplate DNA strand had Biotin attached at the 5′ end via a C6-amino linker. The biotin was used in the single-molecule experiments for immobilization of the elongation complex. The template DNA strand contained an internal C6-amino linker attached to a thymidine residue at either position −10 (DNA1) or position +3 (DNA2). Alexa647 (Molecular Probes) then was covalently attached to these positions by using an *N*-hydroxysuccinimidylester derivative following the manufacturer's suggestions. Labeled DNA oligomers were purified by HPLC.

In addition to the FRET measurements of complexes with labeled RNA, control experiments were performed to measure the distance between donor dye on the DNA and acceptor on Rpb7. To this end, the template strand was labeled at position −10 (DNA1) or at position +3 (DNA2) with 5-TMR isothiocyanate (TRITC; Molecular Probes) followed by HPLC purification. Furthermore, the Alexa-647-labeled Rpb7–C150, biotin-labeled nontemplate DNA, and a nonlabeled 17-nt RNA primer were used in the preparation of elongation complexes for these test experiments.

DNA–RNA scaffolds were annealed by using equimolar amounts of template DNA, nontemplate DNA, and RNA in TE buffer (10 mM Tris·HCl/1 mM EDTA) at a final concentration of 1 μM. The mixture was heated to 95°C for 5 min, followed by fast cooling to 55°C and then slow cooling to 4°C in 1 h. The Pol II–DNA–RNA–Rpb4/7 complex was assembled as described in ref. 3. The complex was purified using Microcon YM100 centrifugal filter units (Millipore) against assembly buffer.

Preparation of Sample Chamber for sp-FRET Measurements. Quartz slides (Finkenbeiner) and coverslips (Marienfeld) were thoroughly cleaned with the detergent Hellmanex II (Hellma) and dried in nitrogen flow. Remaining particles were oxidized with a butane-gas torch. Afterward the quartz slides were silanized by using 2% (vol/vol) (3-aminopropyl)-triethoxysilane (Sigma-Aldrich) in acetone, followed by desiccation, rinsing with water, and drying. Hereafter, a solution of mPEG-succinimidyl propionate [15% (wt/vol), M_r 5,000 Da, Nektar Therapeutics] and biotinylated PEG–*N*-hydroxysuccinimide ester (PEG-NHS) [1% (wt/vol), M_r 3,400 Da, Nektar Therapeutics] in carbonate–bicarbonate buffer (pH 9.4) was applied. Subsequently the PEGylated slides were cleaned with water and dried.

The slides then were assembled together with a precut sealing film (Nescofilm) and a cleaned coverslip and heated to 150°C for 1 min to allow for the thermoplastic film to seal a channel and produce a microfluidic chamber. Two holes drilled into the quartz slides were used to insert and remove fluids from the chamber.

Pol II elongation complexes were attached to the biotin–PEG surface of the microfluidic chamber via neutravidin/biotin attachment. To this end, the chamber was incubated with 0.5 mg/ml neutravidin (Molecular Probes) in PBS. After exchanging the buffer with assembly buffer, the preassembled elongation complexes were loaded. Afterward unbound complexes were removed by washing extensively with assembly buffer.

Experimental Setup for sp-FRET. sp-FRET experiments were performed on a homebuilt prism-based total internal reflection fluorescence microscope (TIRFM). In this apparatus, the sample is excited by using both a frequency-doubled Nd-YAG laser (Crystalaser) at 532 nm for the excitation of donor molecules and FRET pairs and a He-Ne laser (Uniphase) at 633 nm for the direct excitation of the acceptor. The light from the two lasers is combined spatially with a dichroic mirror (Chroma Z532RDC). During the measurement, the excitation can be alternated between the two laser sources by using two software-controlled shutters (Uniblitz LS6). Alternating between FRET and direct-acceptor excitation allows for the discrimination of dynamics in FRET efficiencies caused by conformational changes against changes in FRET efficiencies caused by fluctuations in acceptor brightness (18) (see *SI Text*).

The excitation light is coupled into the sample chamber by means of a small prism. For total internal reflection (TIR), the incident angle is adjusted to ≈74°. The interior surface of the flow chamber sits at the focus of a lens with focal length f = 75 mm, yielding an excitation area of ≈70 × 35 μm^2 with a power density of 1.5$\mu W/\mu m^2$. Fluorescence intensity is collected via a water-immersion objective (Plan Apo ×60, N.A. 1.2; Nikon) and directed to an intensified back-illuminated electron-multiplying charge-coupled device (EMCCD) camera (iXon

DV887DCS-BV; Andor). To detect both donor and acceptor fluorescence simultaneously with the same camera, one half of the CCD chip is physically blocked by using a slit in the image plane of the detection path. Two channels of detection then are introduced by splitting and spatially offsetting the donor and acceptor fluorescence via a dichroic beam splitter (Chroma 645DCXR). Emission filters are placed in the two detection paths centered at 580 nm (Omega Optical 3RD550–610) and 710 nm (Chroma HQ710/100M) to isolate the fluorescence light of the donor and acceptor molecules, respectively. All measurements were recorded with an exposure time of 100 ms per frame for a 30-s duration.

Data Analysis. The acquired data were analyzed by using custom software written in MATLAB. We used a fully automated routine to find FRET pairs and to calculate and subtract the local background. For the calculation of FRET efficiency of the individual FRET pairs, we used the following formula (44):

$$E = \frac{I_A - \beta \cdot I_D}{I_A + \gamma \cdot I_D}, \qquad [1]$$

where

$$\gamma = \frac{I_A - I'_A}{I'_D - I_D}$$

and

$$\beta = \frac{I'_A}{I'_D}.$$

I_A and I_D are background-corrected intensities from the acceptor and donor channels and I_A/I_D and I'_A/I'_D are the intensities before and after acceptor photobleaching, respectively. β and γ are experimental correction factors: β accounts for the leakage of the donor emission into the acceptor channel, and γ is a factor that includes the quantum yields of the fluorophores and the detection efficiencies of the two channels. We determined the correction factors for all FRET pairs individually by time-averaging the intensities I and I'. FRET pairs where no acceptor bleaching was observed were discarded from the analysis, because for these FRET pairs γ could not be determined. Direct excitation of the acceptor was so low (<5%) that it did not lead to detectable changes in the histograms (ΔE <1%) and therefore was disregarded in the analysis. FRET efficiencies were calculated for every time point after filtering the original data sets by using a 10-point sliding-average filter. The histograms of these FRET values represent transfer efficiency distributions and describe dynamics of nascent RNA products. Although most of the observed histograms show a fairly narrow distribution (width ≈0.2), there are some examples of broadened histograms, which could be caused, for example, by a lower signal or an increased mobility of the RNA.

From the FRET efficiencies, we computed distances using the following equation:

$$d = R_0\left(\frac{1}{E} - 1\right)^{\frac{1}{6}}, \qquad [2]$$

where R_0 is the Förster radius. We used a standard procedure (45) to determine R_0 experimentally by measuring the donor quantum yield (using rhodamine 101 as a standard) and donor emission and acceptor absorption spectra (to compute the overlap integral) and assuming a free diffusion of the dye molecule (*SI Text*).

Different effects such as dye-linker structure and dynamics, uncertainties in R_0, and dynamics of the RNA itself all contribute to the experimental error. The precise error of the measurement therefore can only be estimated. The experimental tests performed in this work (comparison of experimentally determined distances to distances known from the crystal structure and comparison of fourth measured distance to expected distance) yielded errors <5 Å. Therefore, we assume an experimental error of ≈5 Å throughout this work.

Trilateration. For each RNA length, we computed three distances using the three recorded histograms. To infer from these three distances the unknown relative position of the dye molecule, we mathematically construct a sphere around each of the three known positions with a radius determined by the FRET measurement. For the attachment points on DNA1 and DNA2, we used the position of the C6 atom, and in the case of the labeling sites on Rpb7, we used the position of the respective sulfur atom as the center of the sphere. The intersection point of the three spheres determines the unknown position (20). It should be noted that mathematically there might be as many as two intersection points; however, one of these points can be ruled out because of distance constraints, that is, the RNA simply is not long enough to reach the second point. Alternatively, the right intersection point can be determined by measuring a fourth distance.

ACKNOWLEDGMENTS. We thank Marta Blamowska for help in determining the Förster radii, Peter Schwaderer for help with the trilateration procedure, Johannes Gierlich and Thomas Carell for the HPLC purification of labeled DNA, Anass Jawhari for the expression and purification of TFIIB, Hazen Babcock for helpful discussions regarding the data analysis, and Christoph Bräuchle and Don Lamb for fruitful discussions. The work was supported by the Deutsche Forschungsgemeinschaft (SFB 646), the Nanosystems Initiative Munich, and the Center for Nanoscience (CeNS) at Ludwig-Maximilans-Universität München.

1. Cramer P, Bushnell DA, Kornberg RD (2001) *Science* 292:1863–1876.
2. Armache KJ, Mitterweger S, Meinhart A, Cramer P (2005) *J Biol Chem* 280:7131–7134.
3. Kettenberger H, Armache KJ, Cramer P (2004) *Mol Cell* 16:955–965.
4. Westover KD, Bushnell DA, Kornberg RD (2004) *Cell* 119:481–489.
5. Armache KJ, Kettenberger H, Cramer P (2005) *Curr Opin Struct Biol* 15:197–203.
6. Gnatt AL, Cramer P, Fu J, Bushnell DA, Kornberg RD (2001) *Science* 292:1876–1882.
7. Westover KD, Bushnell DA, Kornberg RD (2004) *Science* 303:1014–1016.
8. Korzheva N, Mustaev A, Kozlov M, Malhotra A, Nikiforov V, Goldfarb A, Darst SA (2000) *Science* 289:619–625.
9. Cramer P, Bushnell DA, Fu J, Gnatt AL, Maier-Davis B, Thompson NE, Burgess RR, Edwards AM, David PR, Kornberg RD (2000) *Science* 288:640–649.
10. Ujvari A, Luse DS (2006) *Nat Struct Mol Biol* 13:49–54.
11. Sosa H, Peterman EJ, Moerner WE, Goldstein LS (2001) *Nat Struct Biol* 8:540–544.
12. Yildiz A, Forkey JN, McKinney SA, Ha T, Goldman YE, Selvin PR (2003) *Science* 300:2061–2065.
13. Zhuang X, Bartley LE, Babcock HP, Russell R, Ha T, Herschlag D, Chu S (2000) *Science* 288:2048–2051.
14. Schmidt T, Schutz GJ, Baumgartner W, Gruber HJ, Schindler H (1996) *Proc Natl Acad Sci USA* 93:2926–2929.
15. Ha T, Enderle T, Ogletree DF, Chemla DS, Selvin PR, Weiss S (1996) *Proc Natl Acad Sci USA* 93:6264–6268.
16. Weiss S (1999) *Science* 283:1676–1683.
17. Brueckner F, Hennecke U, Carell T, Cramer P (2007) *Science* 315:859–862.
18. Kapanidis AN, Lee NK, Laurence TA, Doose S, Margeat E, Weiss S (2004) *Proc Natl Acad Sci USA* 101:8936–8941.
19. Muller BK, Zaychikov E, Brauchle C, Lamb DC (2005) *Biophys J* 89:3508–3522.
20. Rasnik I, Myong S, Cheng W, Lohman TM, Ha T (2004) *J Mol Biol* 336:395–408.
21. Hillisch A, Lorenz M, Diekmann S (2001) *Curr Opin Struct Biol* 11:201–207.
22. Vassylyev DG, Vassylyeva MN, Perederina A, Tahirov TH, Artsimovitch I (2007) *Nature* 448:157–162.
23. Nudler E (1999) *J Mol Biol* 288:1–12.
24. Pal M, Luse DS (2002) *Mol Cell Biol* 22:30–40.
25. Pal M, Luse DS (2003) *Proc Natl Acad Sci USA* 100:5700–5705.
26. Ujvari A, Pal M, Luse DS (2002) *J Biol Chem* 277:32527–32537.
27. Proudfoot NJ, Furger A, Dye MJ (2002) *Cell* 108:501–512.
28. Bushnell DA, Westover KD, Davis RE, Kornberg RD (2004) *Science* 303:983–988.
29. Chen HT, Hahn S (2003) *Mol Cell* 12:437–447.
30. Pal M, Ponticelli AS, Luse DS (2005) *Mol Cell* 19:101–110.
31. Kapanidis AN, Margeat E, Ho SO, Kortkhonjia E, Weiss S, Ebright RH (2006) *Science* 314:1144–1147.
32. Dietz H, Rief M (2006) *Proc Natl Acad Sci USA* 103:1244–1247.
33. Kapanidis AN, Margeat E, Laurence TA, Doose S, Ho SO, Mukhopadhyay J, Kortkhonjia E, Mekler V, Ebright RH, Weiss S (2005) *Mol Cell* 20:347–356.
34. Margeat E, Kapanidis AN, Tinnefeld P, Wang Y, Mukhopadhyay J, Ebright RH, Weiss S (2006) *Biophys J* 90:1419–1431.
35. Coban O, Lamb DC, Zaychikov E, Heumann H, Nienhaus GU (2006) *Biophys J* 90:4605–4617.
36. Adelman K, La Porta A, Santangelo TJ, Lis JT, Roberts JW, Wang MD (2002) *Proc Natl Acad Sci USA* 99:13538–13543.
37. Forde NR, Izhaky D, Woodcock GR, Wuite GJ, Bustamante C (2002) *Proc Natl Acad Sci USA* 99:11682–11687.
38. Shaevitz JW, Abbondanzieri EA, Landick R, Block SM (2003) *Nature* 426:684–687.
39. Abbondanzieri EA, Greenleaf WJ, Shaevitz JW, Landick R, Block SM (2005) *Nature* 438:460–465.
40. Thomen P, Lopez PJ, Heslot F (2005) *Phys Rev Lett* 94:128102.
41. Skinner GM, Baumann CG, Quinn DM, Molloy JE, Hoggett JG (2003) *J Biol Chem* 279:3239–3244.
42. Harada Y, Ohara O, Takatsuki A, Itoh H, Shimamoto N, Kinosita K, Jr (2001) *Nature* 409:113–115.
43. Galburt EA, Grill SW, Wiedmann A, Lubkowska L, Choy J, Nogales E, Kashlev M, Bustamante C (2007) *Nature* 446:820–823.
44. Sabanayagam CR, Eid JS, Meller A (2005) *J Chem Phys* 123:224708.
45. Vamosi G, Gohlke C, Clegg RM (1996) *Biophys J* 71:972–994.
46. Pettersen EF, Goddard TD, Huang CC, Couch GS, Greenblatt DM, Meng EC, Ferrin TE (2004) *J Comput Chem* 25:1605–1612.